TUDelft

Delft University of Technology

Time-resolved PIV investigation of the secondary instability of cross-flow vortices

Serpieri, Jacopo; Kotsonis, Marios

Important note
To cite this publication, please use the final published version (if applicable).
Please check the document version above.

Time-resolved PIV investigation of the secondary instability of cross-flow vortices

Jacopo Serpieri

AWEP Department-Aerodynamics, TU Delft
Kluyverweg 1, 2629HS Delft, The Netherlands
j.serpieri@tudelft.nl

Marios Kotsonis

AWEP Department-Aerodynamics, TU Delft
Kluyverweg 1, 2629HS Delft, The Netherlands
m.kotsonis@tudelft.nl

ABSTRACT

Time-resolved PIV measurements of the secondary instability modes of cross-flow vortices are presented. Measurements are performed on a large scale 45° swept wing at chord Reynolds number of 2.17 million in a low turbulence wind-tunnel facility. Using acquisition frequencies of 20 kHz, the present study is the first experimental demonstration of spatio-temporally resolved measurements of these structures. Statistical and spectral analysis reveals a fluctuating velocity field, strongly conditioned in space by the primary stationary cross-flow vortex. The flow structures related to the *type-I* high-frequency instability and *type-III* are captured by Proper Orthogonal Decomposition of the instantaneous flow-fields. Their temporal evolution is analysed showing good agreement with previous studies thus confirming that POD is correctly representing the flow structures of the relevant instability modes. The low frequency meandering oscillation of the stationary vortices, first reported by Serpieri & Kotsonis (2016*b*), is observed and characterised.

INTRODUCTION

The main instability mechanism triggering boundary layer laminar-to-turbulent transition on swept wings is the cross-flow (CF) instability (Saric *et al.*, 2003). This is directly caused by the secondary flow, orthogonal to the inviscid streamline, taking place in three-dimensional boundary layers.

In low free stream turbulence environments such as free flight, this instability manifests as stationary co-rotating vortices roughly aligned with the flow (Bippes, 1999). The footprint of the stationary vortices typically appears as a sequence of streamwise aligned streaks of high and low wall shear in flow visualisation studies Dagenhart *et al.* (1989). These vortices experience growth along the streamwise direction deeply modifying the boundary layer. Due to the modification of the boundary layer, strong velocity shears develop, which are subject to secondary high-frequency instability (Kohama *et al.*, 1991) of Kelvin-Helmholtz type (Bonfigli & Kloker, 2007). Several efforts have been dedicated to the study of this mechanisms in the last 30 years. Due to the relatively high frequency and small wavelength of the secondary structures, hot-wire measurements are typically the measurement technique of choice (e.g. Kohama *et al.* (1991) and White & Saric (2005)). Additionally, secondary linear stability theories were used by e.g. Fischer & Dallmann (1991), Malik *et al.* (1999) and Koch *et al.* (2000) to predict pertinent features of the instabilities such as growth and wavelength. These theories make use of pre-computed distored base flows, which include the effect of the primary vortex a-priori. Finally, Direct Numerical Simulations (DNS) were performed by e.g. Högberg & Henningson (1998); Wassermann & Kloker (2002) and Bonfigli & Kloker (2007).

Experimentally, the description of the unsteady secondary cross-flow instabilities presents significant challenges, given the very high frequency and narrow wavelength of these modes, thus restricting available measurements. The vast majority of these is based on time-resolved point measurements (HWA), which are usu-ally uncorrelated in space. To date and to the authors knowledge, only the studies of Kawakami *et al.* (1999); Chernoray *et al.* (2005) and Serpieri & Kotsonis (2016*a*) have been successful in measuring the spatio-temporal evolution of the instability waves. This was achieved by conditioning and subsequent phase-reconstruction of the hot-wire signal by artificially forcing the boundary layer at deterministic frequencies and phases. This approach overcomes the limitation encountered in previous experimental studies regarding the lack of spatio-temporal correlation. However, it encompasses two main limiting assumptions. First, only the unsteady field components which are directly correlated to the forcing signal can be resolved, limiting the analysis to single frequency instabilities. Second, the boundary layer is forced by an external mechanism. This implies that the amplitude of the forcing might alter the natural growth and transition evolution. As such a further limitation of this technique is the restriction of the forcing amplitude to as small as possible in order to lock the unsteady field without modifying its evolution (Serpieri & Kotsonis, 2016*a*).

Recently, the authors employed tomographic-PIV to inspect the boundary layer of a swept wing subject to cross-flow instability (Serpieri & Kotsonis, 2016*b*) . Proper Orthogonal Decomposition (POD) of the captured flow-fields led to the identification of the unsteady flow structures related to the secondary instability mechanisms arising on the primary stationary vortices. Additionally to the well known *type-I* and *type-III* modes (Koch *et al.*, 2000), a previously unknown, highly energetic global oscillation mode was identified. This was attributed to a low frequency 'shake' of the stationary cross-flow vortex, which in turn could originate in upstream oscillations of the external flow. While the study of Serpieri & Kotsonis (2016*b*) provided significant insight to the spatial arrangement of the primary and secondary instabilities, the low sampling frequency of that experiment did not allow the direct investigation of the temporal evolution of the high frequency travelling waves. This was indirectly estimated from the tomo-PIV fields applying the Taylor hypothesis on flow convection and compared to the HWA measurements.

To overcome the above mentioned limitations, the present study provides an effort towards a more complete spatio-temporal description of the pertinent unsteady structures in the vicinity of the stationary cross-flow vortex. To this goal, planar two-component, high-speed PIV is deployed. The investigated domain lies on a wall-parallel plane and concentrates on a small chordwise portion of a single cross-flow vortex (CFV) undergoing turbulent breakdown.

EXPERIMENTAL SETUP
Model, wind-tunnel and Reference System

The model used in the current investigation is a 45 degrees swept wing (the angle of sweep is defined with Λ) of about 1.25m of span and 1.27m of chord in the free stream direction (c_X). The airfoil used is a modified version of the NACA 66018 shape, named 66018-M3J (Serpieri & Kotsonis, 2016*b*).

The wind-tunnel where the experiments were performed is the

TU Delft LTT facility: a closed loop, low turbulence subsonic tunnel with a testing chamber of 1.25m × 1.80m of height and width respectively and 2.6m long. The tunnel presents seven anti-turbulence screens and a contraction ratio of 17:1. The turbulence intensity measured with a hot-wire sensor whose signal is bandpass filtered between 2Hz and 5000Hz is Tu/U_∞=0.07 at the free stream velocity U_∞=24m/s. This value is low enough to observe stationary cross-flow waves (see Bippes (1999)) and indeed this was the case for the test case, $U_\infty = 25.6m/s$ and Reynolds $Re = 2.17 \cdot 10^6$ (see also Serpieri & Kotsonis (2016b)). The experiment was performed at incidence of $\alpha = 3°$ and the flow over the wing pressure side was investigated. For this flow configuration, the measured pressure minimum point is at $X/c_X = 0.63$. Spanwise-invariance flow conditions were demonstrated by Serpieri & Kotsonis (2015) even without installation of streamlined wall liners.

Following Reibert *et al.* (1996) and White & Saric (2005), the developing cross-flow instability was conditioned to a single spanwise wavelength by triggering, with micrometric roughness elements (diameter 2.8mm, height 10μm) at the leading edge (X/c_X=0.025), the naturally dominant mode (frequency: f=0, spanwise-wavelength: λ^f=9mm) (Serpieri & Kotsonis, 2016b). The monochromatic forcing together with the invariance of the flow along the leading edge direction, make the measurement of the flow-field pertaining to a single vortex, valid for the entire field at the same chordwise position (White & Saric, 2005).

The results are presented in the un-swept coordinate system. This is defined with the upper case letters XYZ and is such that the X and Y axis lie in an horizontal plane (the X being in the chord plane and Y orthogonal to that plane) while the Z is the vertical direction. The velocity components along this coordinate system are indicated with upper case letters UVW. In the vertical Z direction, the forced wavelength is $\lambda_Z^f = \lambda^f \cos(\Lambda)$=6.36mm. This quantity is used as length scale for the Z axis while the chord (c_X=1.27m) is used for the X axis.

Particle Image Velocimetry

Particle image velocimetry was used to inspect the boundary layer velocity field. The inspected plane is aligned to the $X - Z$ directions and is positioned at 1.5mm from the model surface. The measurement region is centred with the station $X/c_X = 0.545$.

The PIV experiment setup is presented in figure 1a. As shown, the camera was looking from outside the wind-tunnel through opportune optical windows. It was placed at approximately 1m from the measured plane. The camera used in this experiment is a *Lavision Imager HS* featuring a sensor of 2016×2016px^2, pixel size of 11μm and 12bits of digital resolution. However in order to increase the acquisition frame rate, the camera's active sensor was reduced to 348×176px^2 for the current experiment. The camera was equipped with a *Nikon Nikkor 200mm micro* lens operated at $f_\sharp$=5.6. The resulting magnification factor of the PIV experiment is M=0.24. Illumination was provided from downstream as shown in the schematic. A Nd:YAG high speed *Continuum Mesa PIV* (18mJ per pulse) was employed. The light beam was opportunely shaped into a sheet less than 1mm thick. The light sheet was oriented such to be parallel to the model surface. The flow was seeded using *Safex* water glycol injected downstream of the testing chamber. The average particle diameter is 1μm.

Cross-correlation was performed with final interrogation windows of 24×24px^2 with relative overlap set to 75%. As such, the final vector spacing was approximately 0.18mm in both X and Z. The time interval between the two pulses was set to 15μs thus leading to average particles displacement in the free stream of $\approx$10px. The system was operated at the very high frequency of 20kHz and a sequence of 65000 image pairs was acquired thus the total sampling
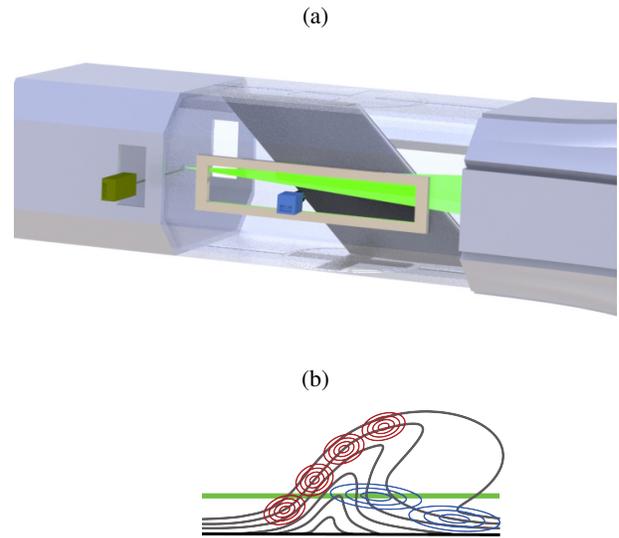

(a)

(b)

Figure 1: (a) Schematic of the PIV setup. The flow comes from right. The camera (blue) looks at the illuminated region (light green) from outside the testing chamber (drawn semi-transparent) through opportune optical windows. The laser head is shown (dark green) and illumination comes from downstream. (b) Schematic of the laser sheet (light green) w.r.t. the primary cross-flow vortex (grey) and *type-I* (red) and *type-III* (blue) secondary modes. Perspective from upstream. Schematics not to scale

time was 3.25s.

DISCUSSION

Time-resolved PIV allows direct inspection of the spatio-temporal evolution of the unsteady flow structures. Additionally, the extended sampling time of the current experiment leads to converged statistic fields. In figure 2(a), the time-averaged ($\bar{U}$) and standard deviation (U_{RMS}) velocity fields are shown. The contour presents a cross-cut plane, at 1.5mm from the model surface, of a stationary cross-flow vortex at the streamwise location corresponding to its turbulent breakdown (Serpieri & Kotsonis, 2016b). In figure 1b, a schematic shows the measurement plane with respect to the analysed flow structures. The lower part (Z/λ_Z^f¡0.3) of the velocity field is the high-speed region in-between neighbouring vortices. In the upper part of the field, a low-speed region occurs that corresponds to the upwelling flow, shifted upwards by the stationary vortex. The second velocity minimum in the contour shows instead the downwelling flow, associated to the falling lobe of the primary waves. The fluctuations are stronger in the high-shear regions as reported in literature (e.g Malik *et al.* (1999); Wassermann & Kloker (2002); White & Saric (2005)).

In order to facilitate inspection of the spectral content of the flowfield, the full time series of the $U-$ velocity fluctuations is sampled along the constant-chord segment AB of figure 2(a) and Fourier frequency-transformed. The modified periodogram method of Welch (Welch, 1967) is used. The spectra have a final resolution of 10Hz. The results are presented in figure 2(b). High spectral energy density is observed at very low frequencies and throughout the extension of the stationary vortex. Serpieri & Kotsonis (2016b) reported a low frequency spanwise oscillation of the stationary vortices encompassing most of the turbulent kinetic energy (TKE). This phenomenon was not observed in previous literature as no spatially

correlated measurements were available for this type of flows (recall that the works of Kawakami *et al.* (1999), Chernoray *et al.* (2005) and Serpieri & Kotsonis (2016*a*) resolved only the forced mode). The cause of this meandering of the stationary waves, which, as for the current study, were forced with leading edge roughness, could not be retrieved. Serpieri & Kotsonis (2016*b*) suggested a low frequency oscillation of the attachment line, a shift imposed by the wind-tunnel boundary layer at the wing tips or a vortical self-induced motion as possible explanations. Serpieri & Kotsonis (2016*b*) commented that such this oscillation has likely no effects on the transition evolution given its very low frequency.

The spectra of figure 2(b) indicate very high fluctuation energy between 0 and 10Hz. It is likely that this energy pertains to the described meandering of the stationary waves and it will be further inspected in the remainder of this analysis. The frequency band 10Hz$\leq f \leq$400Hz also features high energy levels. It can be conjectured that the *type-III* mode is the main driver of this particular range. This mode was shown to originate by the interaction between the primary stationary and primary travelling waves (e.g. Fischer & Dallmann (1991) andMalik *et al.* (1999)). Finally, a third area of significant spectral energy is centred at f=4.5kHz. This band is related to the secondary instability modes generated by the perturbation of the stationary velocity shears (Bonfigli & Kloker, 2007). Moreover, fluctuations are spreading throughout the spectrum reaching, with still high energy, the highest resolved frequency (i.e. 10kHz). The measurement location is at the stationary vortex breakdown and therefore the turbulent energy cascade is setting in.

Following previous work by the authors (Serpieri & Kotsonis, 2016*b*), Proper Orthogonal Decomposition (POD) of the instantaneous velocity fields is performed to highlight the coherent flow structures. The snapshot POD approach (Sirovich, 1987) is exploited. The turbulent kinetic energy (TKE) distribution of the first 20 modes is shown in figure 3 in both absolute values and relative (w.r.t the total sum) cumulative sum. The first POD mode appears at significant levels of energy. This mode replicates the POD mode 1 reported by Serpieri & Kotsonis (2016*b*) as it will be shown later. The remainder POD ensemble indicates the cascade of energy with the first 31 POD modes (not shown) encompassing more than 50% of the total TKE.

Several POD modes appear paired as indicated by similar energy levels (e.g. Φ_2-Φ_3, Φ_4-Φ_5, Φ_8-Φ_9). Mode pairs in relative phase quadrature are indicative of advecting structures (Van Oudheusden *et al.*, 2005). Serpieri & Kotsonis (2016*b*), reported two pairs of modes that were harmonically coupled, comparing the flow topology and estimating the mode frequency from the extracted wavelengths, to *type-III* and *type-I* mechanisms. Capitalising on the very high sampling frequency of the current experiment, direct inspection of the modes spectra can be performed. The POD temporal coefficients, derived from the projection of the instantaneous flow-fields on the POD base, are analysed using once again Welch's method. The power spectral density for the first 100 POD modes is shown in the leftmost contour of figure 4. The spectra are estimated to a resolution of 50Hz. It becomes evident that most of the spectral energy density corresponds to the first 20 POD modes, further confirming the POD energy sorting (as from figure 3). The related fluctuations are mainly confined in the band between 0Hz and 5kHz (as shown in figure 2(b)). The rightmost contour of figure 4 offers a magnified view of this region. The first three modes feature the highest energy density. This is contained within the band 0-500Hz. However the first five POD modes have also rather high energy levels up to 2.3kHz. POD modes from 8 to 10 have most of their energy in the band 3.4kHz$\leq f \leq$5.2kHz.

The spectral analysis of the temporal POD coefficients (figure 4), reveals a close proximity of the pertinent spectral bands for the first three POD modes. These are highly energetic modes in a rather low frequency band, suggesting their possible interaction. In a physical context, this suggests the existence of a low-frequency modulation described as a whole by POD modes 1 to 3. The flow structures related to the related POD spatial eigenfunctions are presented in figure 5. POD mode 1 features the same type of structures as the respective POD mode 1 reported by Serpieri & Kotsonis (2016*b*). Two elongated lobes, aligned with the stationary vortex shears, define the footprint of the previously described global oscillation of the cross-flow vortices in the spanwise direction. POD mode 2 has instead a quadrupole structure thus indicating a rotation of the stationary waves (see figure 5(b)). The POD mode 3 showed similar levels of TKE compared to Φ_2 (figure 3). The structure of this mode is in figure 5(c)). It presents a single lobe aligned with the stationary waves but shifted of $\pi/2$ with respect to the structures of Φ_1. From these considerations and recalling that the time-coefficients spectra presented in figure 4 for Φ_1, Φ_2 and Φ_3 occupy the same low-frequency band, it is believed that these three POD modes describe the same flow feature.

As in Serpieri & Kotsonis (2016*b*), roughness elements lock the wavelength of the stationary mode but also its onset and position. Therefore, more than a rigid translation of the stationary waves along the span, the POD modes 1, 2 and 3 refer to a small but highly energetic rotation of the vortices about the roughness element. A short time series reconstruction of the POD modes 1 to 3 is shown in figure 7(a) together with the POD modes eigenfunctions.

POD modes 4 and 5 show structures related to *type-III* modes. These are presented in figure 6. They show elongated structures extending from the outer upwelling side of the stationary waves to the inner downwelling region. The wavelength of this mode was reported by Serpieri & Kotsonis (2016*b*) to be 25mm along the stationary vortices axes. The structures of Φ_4 and Φ_5 have a wavelength of λ_X=14.28mm along the *X* direction. The frequency of the *type-III* mode is centred at 500Hz (Serpieri & Kotsonis, 2016*b*). However, the hot-wire measurements showed a rather broad band around this frequency. The spectrum presented in figure 4 shows a pronounced band centred at 340Hz thus falling in the frequency band of the *type-III* mode. The short time-sequence reconstruction of these POD modes is shown in figure 7(b) allowing to infer their downstream advection, evaluated to be $u_X^c = f\lambda_X$=4.85m/s, and evolution as well as the effect they have on the stationary vortex. Comparing the frequency, the wavelength and the topology of the structures of POD modes Φ_4 and Φ_5, it can be concluded that they are related to the *type-III* instability mode.

The POD mode 8 and 9 and 10 and 13, presented in figure 6, correspond to K-H travelling waves caused by the destabilisation of the strong span-wise shears (Bonfigli & Kloker, 2007). This instability is referred to as *type-I* instability. Kawakami *et al.* (1999); Wassermann & Kloker (2002); Bonfigli & Kloker (2007) and Serpieri & Kotsonis (2016*b*) described them as a train of vortical tubes riding on the outer upwelling flow region of the stationary waves and undergoing massive spatial amplification. The wavelength for this type was evaluated by Serpieri & Kotsonis (2016*b*) to be 4.6mm while the frequency to be centred at 5kHz. The measured wavelengths are λ_X=6.42 and 4.64mm respectively for the two pairs presented in the *X* direction. The frequency of these POD modes pairs is 4kHz for Φ_{8-9} and 4.85kHz for Φ_{10-13}. The phase velocity is u_X^c=25.6m/s for Φ_{8-9} and u_X^c=22.1m/s for Φ_{10-13}. Note that despite the different characteristics of these two pairs of POD modes, the topology and their location with respect to the stationary vortex allow to associate them to the *type-I* mode. Furthermore also for this instability mode, the velocity spectrum shown in figure 4 reported a rather broad hump thus comprising the frequencies of Φ_{8-9} and Φ_{10-13}. The short sequence reconstruction of the pairs
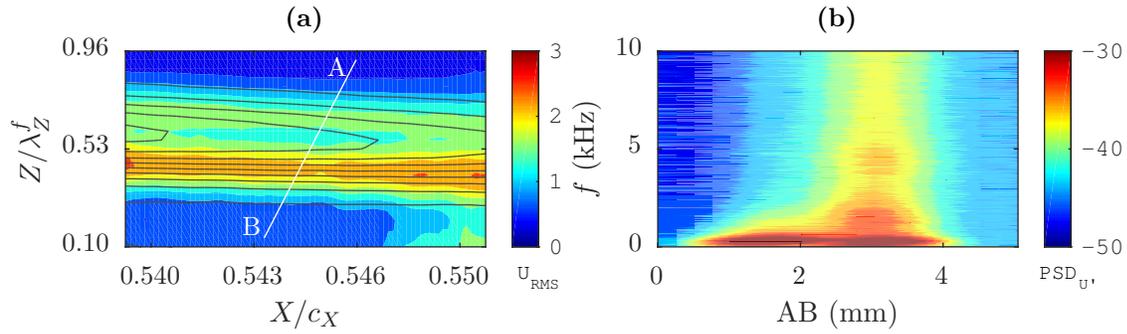
Figure 2: (a) $U-$velocity field: time averaged (solid lines: 11 levels from 18 to 28m/s) and standard deviation (shaded: levels in m/s). The flow comes from left. (b) Power spectral density (δ_f=10Hz) of $U'-$velocity sampled along the constant-chord (at X/c_X=0.545) segment AB (shaded: levels in dB/Hz).
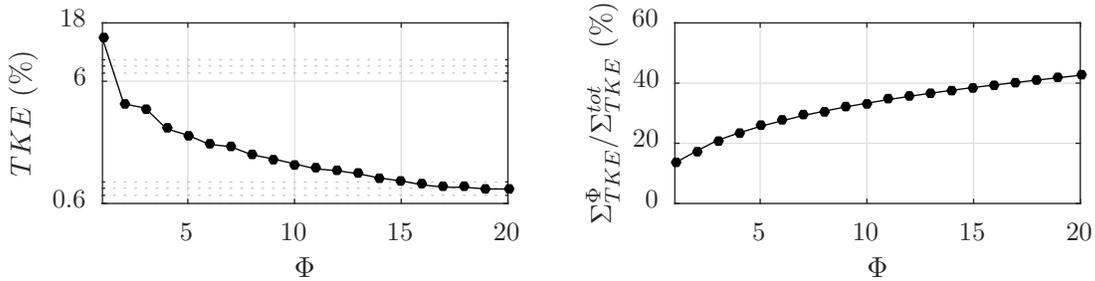

Figure 3: POD turbulent kinetic energy (TKE) distribution: values (left) and relative cumulative sum (right) for the first 20 modes.
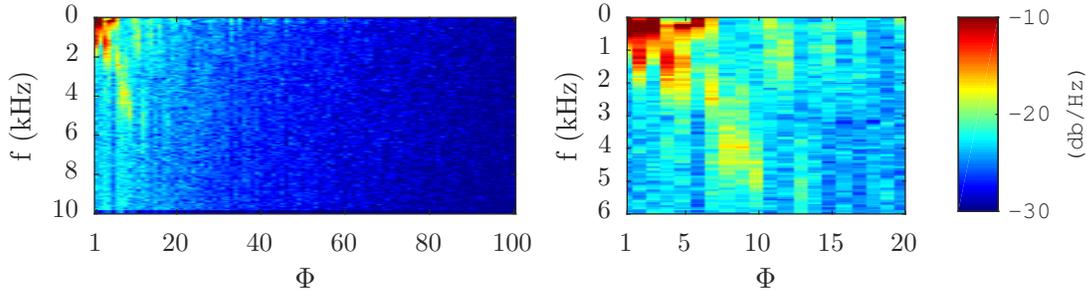

Figure 4: Power spectral density (δ_f=50Hz) of the time coefficients of the first 100 POD modes (left) and magnified view of the first 20 POD modes (right).

of modes Φ_8-Φ_9 and Φ_{10}-Φ_{13} is presented in figure 7(c) and (d), respectively. Again, the downstream advection is evident, confirming the convective nature of these instability mechanisms (Kawakami *et al.*, 1999; Wassermann & Kloker, 2002). Furthermore, it can be seen to what extent, at the measurement location, they perturb the steady shears. This being the indication that the considered boundary layer is undergoing turbulent breakdown.

The analysed properties of the described POD modes are summarized in table 1. Both wavelengths and frequencies agree with the outcomes of the previous low-speed tomo-PIV measurements thus confirming that POD correctly extracts the main flow mechanisms. Moreover, retrieving the frequencies of the modes from the wavelength, applying Taylor's hypothesis, (approach followed by Serpieri & Kotsonis (2016*b*)) is proved to give physical outcomes.

CONCLUSIONS

A swept wing boundary layer undergoing laminar-to-turbulent transition dominated by cross-flow instability mechanisms is investigated with state-of-art flow diagnostics. Planar 2C-PIV at the

very high frequency of 20kHz was employed retrieving the first spatio-temporally resolved measurement of the secondary instability modes arising on and eventually breaking down the stationary cross-flow vortices. Spectral analysis of velocity field showed very high energy in the frequency band comprised between 0 a 400Hz. Moreover higher energy levels were reported centred at 4.5kHz. The fluctuations related to these two bands were inspected by means of proper orthogonal decomposition (POD). The POD modes offered a clear representation of the developing low-frequency *type-III* and high-frequency *type-I* secondary mechanisms. This analysis corroborates and completes the work of Serpieri & Kotsonis (2016*b*) where the POD modes were related to the secondary instability structures by means of Taylor-hypothesis-based comparison with hot-wire measurements. The low-frequency oscillation of the stationary vortices reported by Serpieri & Kotsonis (2016*b*), was observed as well in the present study. Its cause is not assessed and the effect on the transition evolution is likely negligible because of the very low frequency. However, to this mechanism pertain very high levels of turbulent kinetic energy therefore demanding dedi-
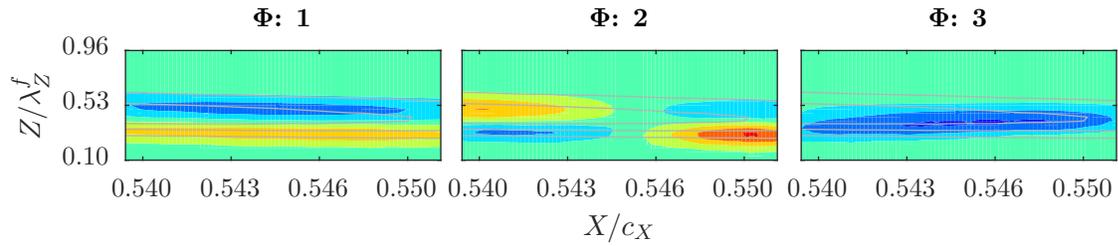
Figure 5: $U-$ velocity field: time averaged (grey lines: 5 levels from 18 to 28m/s) and different normalised POD modes (shaded: 10 levels between ± 0.1).
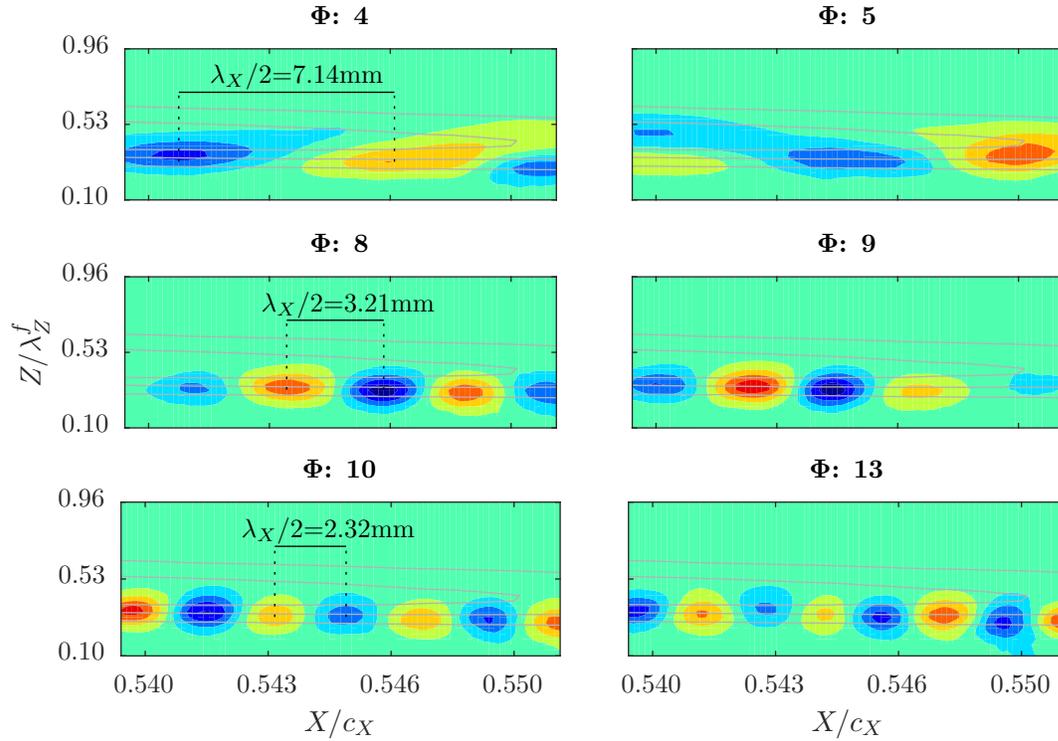

Figure 6: $U-$ velocity field: time averaged (grey lines: 5 levels from 18 to 28m/s) and different normalised POD modes (shaded: 10 levels between ± 0.1).

Table 1: Properties of the analysed POD modes.

POD modes	Instability mode	λ_X(mm)	f(kHz)	u_X^c(m/s)
$\Phi_1 - \Phi_2 - \Phi_3$	*CFVs meandering*	-	0-0.5	-
$\Phi_4 - \Phi_5$	*type-III*	14.28	0.5	4.85
$\Phi_8 - \Phi_9$	*type-I*	6.42	4.00	25.6
$\Phi_{10} - \Phi_{13}$	*type-I*	4.64	4.85	22.1

cated analysis in studies from experimental data (Serpieri & Kotsonis, 2016b).

REFERENCES

Bippes, H. 1999 Basic experiments on transition in three-dimensional boundary layers dominated by crossflow instability. *Progress in Aerospace Sciences* **35** (4), 363 – 412.

Bonfigli, G. & Kloker, M. 2007 Secondary instability of crossflow vortices: validation of the stability theory by direct numerical simulation. *J. Fluid Mech.* **583**, 229–272.

Chernoray, V. G., Dovgal, A. V., Kozlov, V. V. & Löfdahl, L. 2005 Experiments on secondary instability of streamwise vortices in a
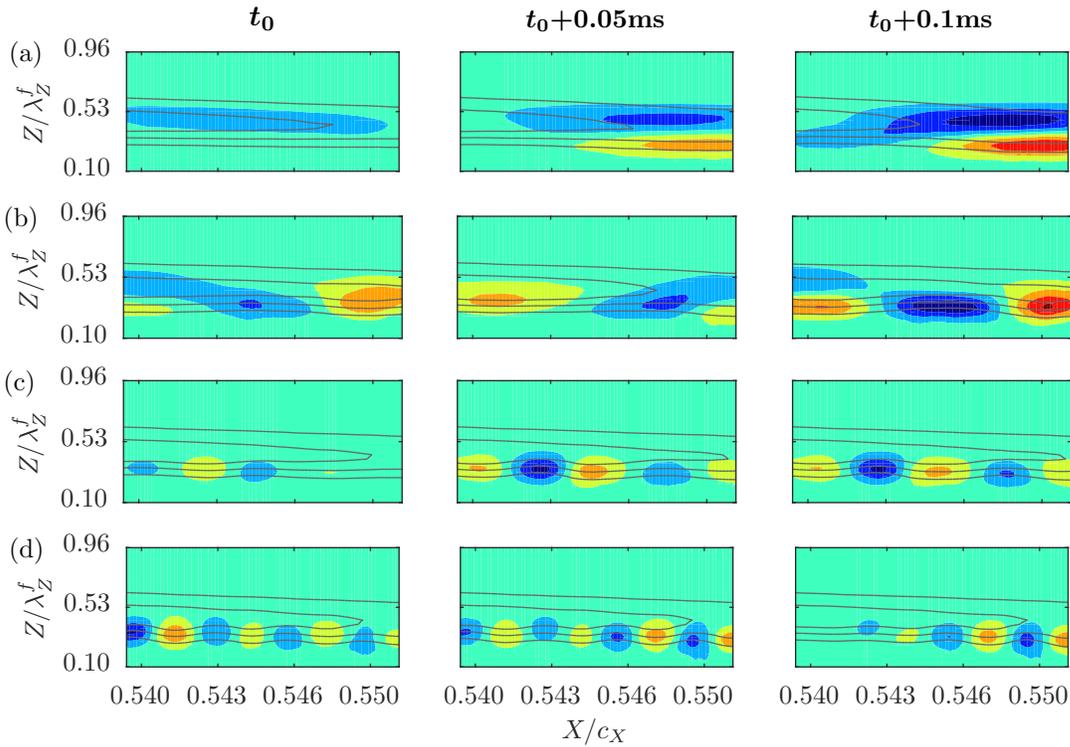
Figure 7: Time series of the $U-$ velocity field: reconstruction from different POD modes with the time-averaged field (grey lines: 5 levels from 18 to 28m/s) and without (shaded: 10 levels comprised between ± 0.12m/s). (a): $\Phi_1 + \Phi_2 + \Phi_3$; (b): $\Phi_4 + \Phi_5$; (c): $\Phi_8 + \Phi_9$; (d): $\Phi_{10} + \Phi_{13}$.

swept-wing boundary layer. *J. Fluid Mech.* **534**, 295–325.

Dagenhart, J. R., Saric, W. S., Mousseux, M. C. & Stack, J. P. 1989 Crossflow vortex instability and transition on a 45-degree swept wing. *AIAA Paper* **89** (1982).

Fischer, T. M. & Dallmann, U. 1991 Primary and secondary stability analysis of a three-dimensional boundary-layer flow. *Physics of Fluids A: Fluid Dynamics (1989-1993)* **3** (10), 2378–2391.

Högberg, M. & Henningson, D. 1998 Secondary instability of cross-flow vortices in falkner-skan-cooke boundary layers. *J. Fluid Mech.* **368**, 339–357.

Kawakami, M., Kohama, Y. & Okutsu, M. 1999 Stability characteristics of stationary crossflow vortices in three-dimensional boundary layer. *AIAA* Paper 1998-811 .

Koch, W., Bertolotti, F. P., Stolte, A. & Hein, S. 2000 Nonlinear equilibrium solutions in a three-dimensional boundary layer and their secondary instability. *J. Fluid Mech.* **406**, 131–174.

Kohama, Y., Saric, W. S. & Hoos, J. A. 1991 A high frequency secondary instability of crossflow vortices that leads to transition. *Proc. R. Aeronaut. Soc. Conf. on Boundary-Layer Transition and Control,* Cambridge, UK .

Malik, M. R., Li, F., Choudhari, M. & Chang, C.-L. 1999 Secondary instability of crossflow vortices and swept-wing boundary-layer transition. *J. Fluid Mech.* **399**, 85–115.

Reibert, M. S., Saric, W. S., Carrillo, R. B. Jr. & Chapman, K. 1996 Experiments in nonlinear saturation of stationary crossflow vortices in a swept-wing boundary layer. *AIAA* Paper 1996-0184 .

Saric, W. S., Reed, H. L. & White, E. B. 2003 Stability and transition of three-dimensional boundary layers. *Annu. Rev. Fluid Mech.* **35** (1), 413–440.

Serpieri, J. & Kotsonis, M. 2015 Design of a swept wing wind tunnel model for study of cross-flow instability. *AIAA* Paper 2015-2576 .

Serpieri, J. & Kotsonis, M. 2016a Spatio-temporal characteristics of secondary instabilities in swept wing boundary layers. *AIAA* Paper 2016-3792 .

Serpieri, J. & Kotsonis, M. 2016b Three-dimensional organisation of primary and secondary crossflow instability. *J. Fluid Mech.* **799**, 200–245.

Sirovich, L. 1987 Turbulence and the dynamics of coherent structures. part i: Coherent structures. *Quarterly of applied mathematics* **45** (3), 561–571.

Van Oudheusden, B.W., Scarano, F., Van Hinsberg, N.P. & Watt, D.W. 2005 Phase-resolved characterization of vortex shedding in the near wake of a square-section cylinder at incidence. *Experiments in Fluids* **39** (1), 86–98.

Wassermann, P. & Kloker, M. 2002 Mechanisms and passive control of crossflow-vortex-induced transition in a three-dimensional boundary layer. *J. Fluid Mech.* **456**, 49–84.

Welch, P. D. 1967 The use of fast fourier transform for the estimation of power spectra: A method based on time averaging over short, modified periodograms. *Audio and Electroacoustics, IEEE Transactions on* **15** (2), 70–73.

White, E. B. & Saric, W. S. 2005 Secondary instability of crossflow vortices. *J. Fluid Mech.* **525**, 275–308.